Compliant joint echogenicity in ultrasound images: towards highly visible steerable needles

van de Berg, Nick; Sánchez-Margallo, Juan A.; Langø, Thomas; van den Dobbelsteen, John

DOI
10.1117/12.2293501

Publication date
2018

Document Version
Final published version

Published in
Medical Imaging 2018

Compliant joint echogenicity in ultrasound images: towards highly visible steerable needles

Nick J. van de Berg, Juan A. Sánchez-Margallo, Thomas Langø, John J. van den Dobbelsteen

Nick J. van de Berg, Juan A. Sánchez-Margallo, Thomas Langø, John J. van den Dobbelsteen, "Compliant joint echogenicity in ultrasound images: towards highly visible steerable needles," Proc. SPIE 10576, Medical Imaging 2018: Image-Guided Procedures, Robotic Interventions, and Modeling, 105760X (19 March 2018); doi: 10.1117/12.2293501

SPIE.

Event: SPIE Medical Imaging, 2018, Houston, Texas, United States

Compliant joint echogenicity in ultrasound images: towards highly visible steerable needles

Nick J. van de Berg*[a], Juan A. Sánchez-Margallo[b,c], Thomas Langø[b], John J. van den Dobbelsteen[a]

[a]Dep. of BioMechnical Engineering, TU Delft, NL, *N.J.P.vandeBerg@TUDelft.nl; [b]Dep. of Medical Technology, SINTEF, NO; [c]Dep. of Computer Systems and Telematics, University of Extremadura, ES.

Abstract Radio frequency ablation is commonly used in the treatment of hepatocellular carcinoma. Clinicians rely on imaging techniques, such as medical ultrasound, to confirm an accurate needle placement. This accuracy may improve by means of active needle steering techniques, which are currently in development. Needle steering will likely increase the clinician's reliance on imaging techniques. This has motivated the study of the echogenicity of steerable needle joint structures. Two needles were manufactured with arrays of kerfs, similar to the compliant joint structures found in steerable needles. The needle visibility was compared to a smooth surface needle and a commercially available RFA needle. The visibility was quantified for both the shaft and tip, by means of a contrast-to-noise ratio (CNR). CNR data were obtained for three insertion angles. The results show that the CNRs of the compliant joint structures were consistently higher than those of the smooth surface needle, whereas they were either higher than or comparable to those of the RFA needle. For acute insertion angles, the bevel tip of the RFA needle had a higher CNR than the conical tip of the kerfed needles, motivating the extension of this visibility study to the full needle design.

Keywords: steerable needle, ultrasonography, visibility, radio-frequency ablation (RFA), contrast-to-noise ratio (CNR), image-guidance, instrument tracking.

INTRODUCTION

The recurrence of hepatocellular carcinoma (HCC) after radio frequency ablation (RFA) is high (>50%) (1). In parts, this may be improved by enhancing the effectiveness of the treatment. The execution of ablation plans is often hampered by irregularities in the thermal treatment effects, as well as the inaccuracies in needle placement (2). In accordance, some safety recommendations for ablation zones include 1 cm tumor-free margins and sufficient overlap of ablation zones for multi-electrode situations (2). The treatment plan execution would benefit from both an increased control over the needle position, as well as an increased awareness of ongoing events.

To increase the control over the size and shape of ablation zones in the treatment of HCC, steerable needles are being developed (3). Needle steering is an active research field, motivated not just by a desire to improve current interventions, but also to increase the spatial reach of these minimally invasive instruments and thereby facilitate new types of treatments (4). Conceivably, steerable RFA needles may access tumors that would otherwise be blocked by vasculature, lung tissue, or other sensitive structures (5). The steerable needle tip design can affect the needle bending forces (6, 7). The design may also affect the needle visibility. Especially for needles with an increased manipulability, visual confirmations of the needle position will become imperative.

Ablation procedures are intrinsically dependent on visual feedback from medical imaging techniques, such as Computed Tomographic (CT), Magnetic Resonance (MR), and Ultrasound (US) imaging. Visual information is used to assess the accuracy in needle placement, to judge the completeness of the treatment and to detect early recurrences (8). The real-time imaging capability of US is valuable for needle tracking during the intervention. In case of isoechoic lesions, image fusion techniques can help to assess the feasibility of a treatment plan (9).

Unfortunately, needles are not always visible in US images. A smooth needle surface will largely reflect sound waves in a specular manner. As a result, the needle visibility depends on the acuteness of the angle between the needle and the ultrasound probe (10), which roughly translates to the needle insertion angle. In addition, the needle visibility may be limited by surrounding tissue with high echogenic properties or shadowing by bone or air (11). Scattered reflections, e.g. resulting from surface irregularities, may be used to increase the needle visibility for a larger set of insertion angles (12).

Medical Imaging 2018: Image-Guided Procedures, Robotic Interventions, and Modeling, edited by Baowei Fei, Robert J. Webster III, Proc. of SPIE Vol. 10576, 105760X · © 2018 SPIE
CCC code: 1605-7422/18/$18 · doi: 10.1117/12.2293501

This study aims to evaluate the visibility of compliant joint structures in US images. These joints – consisting of kerfed patterns in the needle shaft, adjacent to the tip – have been previously used to realize tip-articulated steerable needles (13). The kerfs may additionally increase the local scattering rate of incident US waves. This hypothesis was tested by manufacturing two needles with variations to the compliant joint design. The shaft visibility was compared to a needle with a smooth surface and to a conventional RFA needle, during insertions in a liver tissue mimicking phantom. The visibility was quantified by means of a contrast-to-noise ratio (CNR), which was determined for both the needle shaft and tip and for three insertion angles (20°, 55° and 90°).

METHODS AND MATERIALS

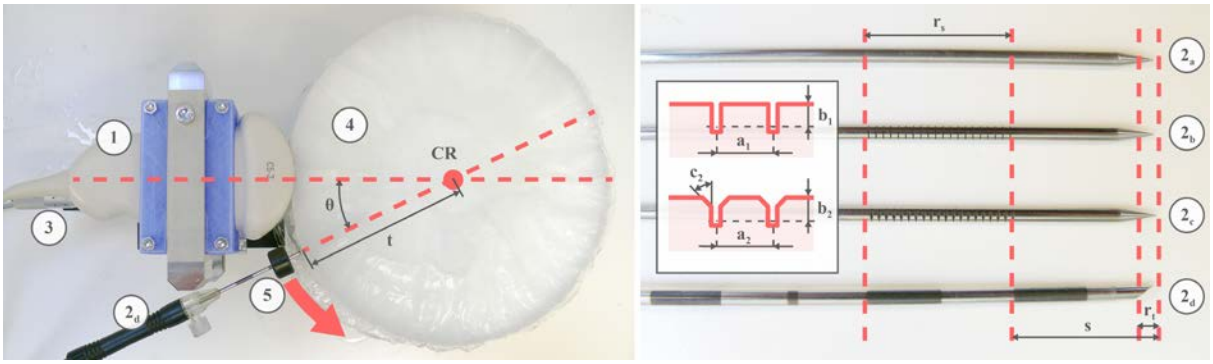

Fig. 1: Overview of the experimental platform, including the 1) US transducer, 2) needle, 3) micro-stage, 4) specimen, and 5) needle guide. Needles were inserted to a depth *t*, and the specimen was rotated (CR = centre of rotation) to an angle θ, before collecting an image. Four needles were analysed, with the subscripts: a) smooth surface, b) kerf type 1, c) kerf type 2, and d) RFA needle. The kerf cross-sections have the dimensions $a_1 = a_2 = 1$ mm, $b_1 = b_2 = 0.5$ mm, and $c_2 = 45° \times 0.2$ mm. The region of interest on the tip and shaft had lengths of $r_t = 2$ mm, and $r_s = 20$ mm, respectively, where $s = 20$ mm.

Measurement setup and needles

The used experimental platform is shown in top-view in Fig. 1. It consisted of an US transducer (C5-2, Philips, NL) on top of a linear micro-stage (PT1/M, Thorlabs, US), and a cylinder-shaped PVA (polyvinyl alcohol) specimen placed on a rotational platform. A needle guide was used to align and vertically distribute the needles during the insertion in the PVA specimen. Variations in the insertion angle were mimicked by rotating the specimen along its cylindrical axis, with CR as the centre of rotation. The specimen diameter was 20 cm and the needles were inserted to a depth, *t* of 10 cm, ensuring that the needle tip and CR approximately coincided. The linear micro-stage was used to slightly press the transducer into the specimen, keeping them in contact, and providing a longitudinal needle view. The transducer could be translated up and down along the specimen by means of an all-thread rod. This facilitated the alignment of the image plane with each hole of the needle guide.

The needles used in this study were custom-made from stainless steel, had a 2 mm diameter, and a conical-shaped tip, as is shown in Fig. 1 (right). One needle had no compliant joint. In two others, kerfs (width = 0.1 mm, depth = 0.5 mm) were introduced adjacent to the tip by means of electric discharge machining. The second kerf type had additional beveled edges (45°×0.2 mm), which may increase specular reflections for certain insertion angles, e.g. close to the 55° angle. A fourth, commercially available RFA needle (Rita Starburst 14 G (2 mm), AngioDynamics, US) was used for comparison.

The specimens were prepared using a 4 m% super hydrolyzed PVA (Selvol PVOH 165, Sekisui Chemical Group NJ, USA), 1 m% scattering agent (Silica gel 60, Merck, DE) in water solution. The specimens were subjected to two freeze-thaw cycles, in accordance with the protocol of (14). This material was selected for its good tissue mimicking properties in US images (15), as well as its resemblance to ex-vivo human liver in terms of the heterogenic, mechanical needle insertion response (14).

The US system (HD7 XE, Philips, NL) was used in combination with a curved array type transducer (C5-2, Philips, NL), which is a conventional choice for interventions procedures, e.g. in the liver. The US system was connected to a capturing device (USB3HDCAP, StarTech, US), enabling the direct acquisition of video files (*.mp4). The system was set to a frequency of 5 MHz to maximize the image resolution. The depth and focus were set to 15 cm and 9 cm, respectively. The gain level was chosen relatively low (Gn = 25) in order to minimize loss of detail caused by image clipping.

Measurement protocol and data processing

Two PVA specimens were prepared. In each specimen, the four needles were inserted five times, in random order. After the needle insertion and the alignment of the imaging plane, the set-up was rotated, with respect to the CR, to mimic insertion angles of 20°, 55°, or 90°. These are the same angles as studied in (11). From each video, multiple frames were collected in proximity to these angles and the best fitting frame was obtained by comparing the line of insertion to a virtual reference line, as is illustrated in Fig. 2.

The frames were analyzed using a manual needle segmentation process, consisting of two graphical coordinate inputs for the needle tip and a well-visible location on the needle shaft. From these inputs, the needle orientation, and the foreground (FG) and background (BG) image samples for the needle tip and shaft, were determined automatically. We used a CNR to quantify the visibility in the US image according to the computational method described in (11):

$$CNR = \frac{|\bar{I}_{FG} - \bar{I}_{BG}|}{\sigma_{BG}}$$

Here, $\bar{I}$ is the mean – and σ the standard deviation – in pixel intensity for a region of interest in the FG or BG. The regions of interest for the needle tip and shaft were sampled in an approach similar to (16). This approach is shown in Fig. 2. The FG for the needle tip was 2 mm in length and 2 mm in width. The FG of the needle shaft was established at 20 mm from the tip, and was 20 mm in length and 2 mm in width. The BG samples were equal in size, but taken directly above the respective FG samples. In case the needle tip or shaft was not visible in the US image, the corresponding CNR value was set to zero, which mathematically equates to the case where $\bar{I}_{FG} = \bar{I}_{BG}$.

For each insertion angle, the CNR data for the shaft and tip of the four needles were analyzed. A Kruskal-Wallis test was performed to analyze the differences in visibility along the four study groups ($p<0.05$) and the differences for each pair of groups were analyzed by means of a post-hoc Mann-Whitney U analysis.

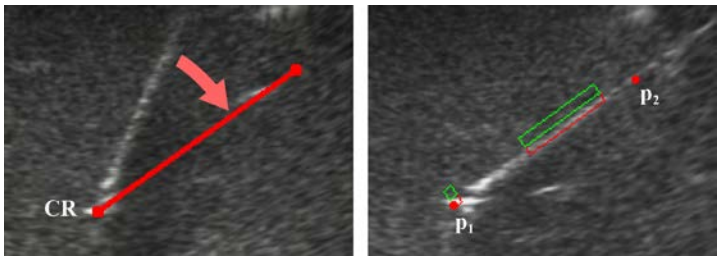

Fig. 2: Zoomed-in sections of US images to illustrate the data processing steps. The specimen was rotated along CR to match the needle insertion line with a virtual reference line (red). Needle segmentation was done manually by clicking on two points (p_1 and p_2), resulting in foreground (red rectangles) and background (green rectangles) samples of the needle tip and shaft.

RESULTS

Examples of the captured images for all combinations of needle types and insertion angles are shown in Fig. 3. The CNR data is summarized in boxplots, indicating a median and standard deviation, in Fig. 4. This figure also includes the results from the statistical analysis. The smooth surface needle (type a) consistently had the lowest CNR for the needle shaft. The compliant joints (types b and c) significantly enhanced this CNR, even for acute insertion angles (20°). The compliant joints yielded a higher CNR than the RFA needle shaft (type d) for the 20° and 55° angles, but not for the 90° angle. For the 20° angle, the tip CNR was significantly higher for the (open) bevel of the RFA needle, compared to any of the (solid) conical tips of the custom-made needles.

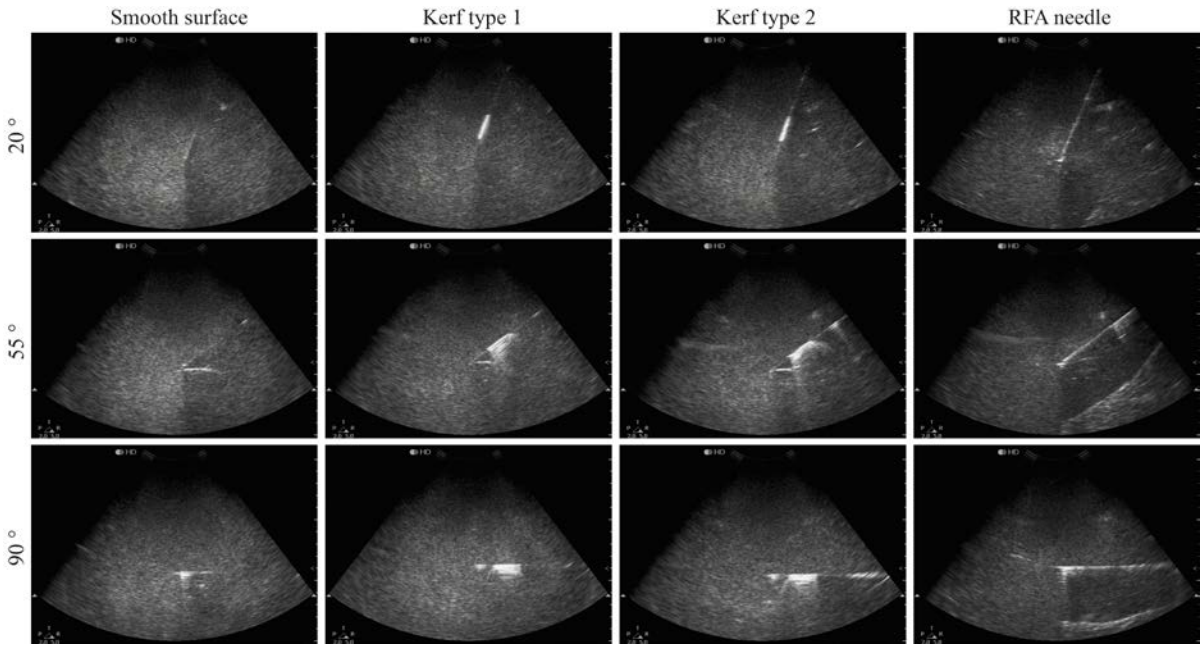

Fig. 3: US images of needles inserted under various insertion angles.

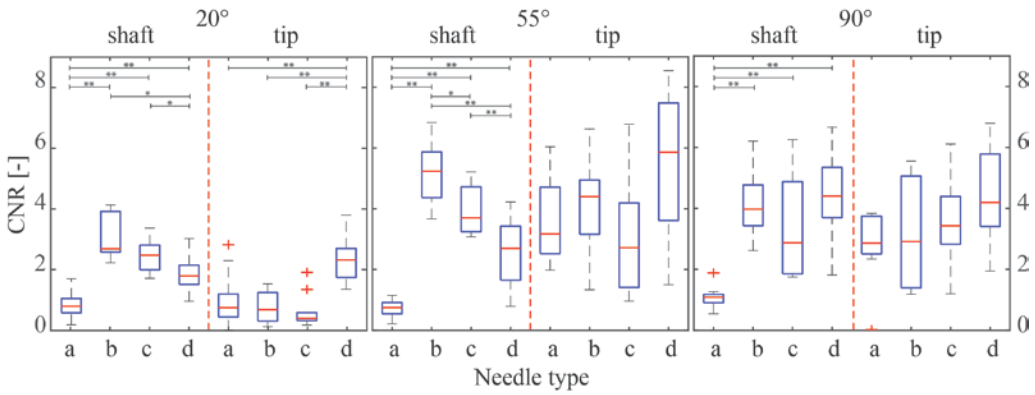

Fig. 4: Boxplots showing the needle shaft and tip visibility, expressed as a CNR, for various insertion angles. The needle is a) smooth surface, b) kerf type 1, c) kerf type 2, or d) RFA needle. Significant differences in CNR values were obtained by means of Mann-Whitney U tests and are indicated, using * for $p<0.05$ and ** for $p<0.01$.

DISCUSSION AND CONCLUSION

This study demonstrates that compliant joint structures increase the local visibility of needles in US images, especially for the more acute insertion angles. At the 90° angle, the visibility was comparable to that of the RFA needle shaft. This was expected, as the rate of return of specular reflections is high at this angle.

An increased visibility helps to find an optimal imaging plane and to estimate the needle location. This is crucial for both closed-loop, vision-based path planners and for manual needle steering applications. In this study, it was found useful to delineate the needle tip and shaft visibility. For acute insertion angles, the bevel tip of the RFA needle was highly visible compared to the solid conical tips. Other tip designs can be evaluated in a similar way to the shaft variations studied in this work.

Notes and disclaimer

This work is completely original and has not been submitted for publication or presentation elsewhere..

REFERENCES

1. Y. Q. Wang et al., "Radiofrequency Ablation versus Hepatic Resection for Small Hepatocellular Carcinomas: A Meta-Analysis of Randomized and Nonrandomized Controlled Trials," *Plos One* **9**(1), (2014).
2. G. D. Dodd et al., "Radiofrequency thermal ablation: Computer analysis of the size of the thermal injury created by overlapping ablations," *Am J Roentgenol* **177**(4), 777-782 (2001).
3. E. C. Burdette et al., "The ACUSITT Ultrasonic Ablator: The First Steerable Needle with an Integrated Interventional Tool," *Proc. SPIE 7629, Medical Imaging 2010: Ultrasonic Imaging, Tomography, and Therapy* (2010).
4. N. J. van de Berg et al., "Design Choices in Needle Steering-A Review," *Ieee-Asme T Mech* **20**(5), 2172-2183 (2015).
5. T. K. Adebar, A. E. Fletcher, and A. M. Okamura, "3-D Ultrasound-Guided Robotic Needle Steering in Biological Tissue," *Ieee T Bio-Med Eng* **61**(12), 2899-2910 (2014).
6. A. M. Okamura, C. Simone, and M. D. O'Leary, "Force modeling for needle insertion into soft tissue," *Ieee T Bio-Med Eng* **51**(10), 1707-1716 (2004).
7. N. J. van de Berg et al., "The influence of tip shape on bending force during needle insertion," *Sci Rep* **7**(40477), (2017).
8. H. Choi et al., "Radio-frequency ablation of liver tumors: Assessment of therapeutic response and complications," *Radiographics* **21**( ), S41-S54 (2001).
9. K. D. Song et al., "Fusion Imaging-Guided Radiofrequency Ablation for Hepatocellular Carcinomas Not Visible on Conventional Ultrasound," *Am J Roentgenol* **201**(5), 1141-1147 (2013).
10. G. A. Chapman, D. Johnson, and A. R. Bodenham, "Visualisation of needle position using ultrasonography," *Anaesthesia* **61**(2), 148-158 (2006).
11. M. Arif, A. Moelker, and T. van Walsum, "Needle Tip Visibility in 3D Ultrasound Images," in *Proc. SPIE 10135, Medical Imaging 2017: Image-Guided Procedures, Robotic Interventions, and Modeling* (2017).
12. K. Nichols et al., "Changes in ultrasonographic echogenicity and visibility of needles with changes in angles of insonation," *J Vasc Interv Radiol* **14**(12), 1553-1557 (2003).
13. N. J. van de Berg, J. Dankelman, and J. J. van den Dobbelsteen, "Endpoint Accuracy in Manual Control of a Steerable Needle," *J Vasc Interv Radiol* **28**(2), 276-283 (2017).

14. T. L. de Jong et al., "PVA matches human liver in needle-tissue interaction," *J Mech Behav Biomed* **69**( ), 223-228 (2017).
15. K. J. M. Surry et al., "Poly(vinyl alcohol) cryogel phantoms for use in ultrasound and MR imaging," *Phys Med Biol* **49**(24), 5529-5546 (2004).
16. K. Nakagawa et al., "Objective and subjective comparison of the visibility of three echogenic needles and a nonechogenic needle on older ultrasound devices," *Acta Anaesthesiol Taiwan* **53**(1), 1-6 (2015).